Two-Dimensional Antimony-Based Perovskite-Inspired Materials for High-Performance Self-Powered Photodetectors

Jianjun Mei, Maning Liu, Paola Vivo, and Vincenzo Pecunia*

The ongoing Internet of Things revolution has led to strong demand for low-cost, ubiquitous light sensing based on easy-to-fabricate, self-powered photodetectors. While solution-processable lead-halide perovskites have raised significant hopes in this regard, toxicity concerns have prompted the search for safer, lead-free perovskite-inspired materials (PIMs) with similar optoelectronic potential. Antimony- and bismuth-based PIMs are found particularly promising; however, their self-powered photodetector performance to date has lagged behind the lead-based counterparts. Aiming to realize the full potential of antimony-based PIMs, this study examines, for the first time, the impact of their structural dimensionality on their self-powered photodetection capabilities, with a focus on 2D $Cs_3Sb_2I_{9-x}Cl_x$ and $Rb_3Sb_2I_9$ and 0D $Cs_3Sb_2I_9$. The 2D absorbers deliver cutting-edge self-powered photodetector performance, with a more-than-tenfold increase in external quantum efficiency (up to 55%), speed of response (>5 kHz), and linear dynamic range (>four orders of magnitude) compared to prior self-powered $A_3M_2X_9$ implementations (A^+: monovalent cation; M^{3+}: Sb^{3+}/Bi^{3+}; X^-: halide anion). Detailed characterization reveals that such a performance boost originates from the superior carrier lifetimes and reduced exciton self-trapping enabled by the 2D structure. By delivering cutting-edge performance and mechanistic insight, this study represents an important step in lead-free perovskite-inspired optoelectronics toward self-powered, ubiquitous light sensing.

J. Mei, V. Pecunia
Jiangsu Key Laboratory for Carbon-Based Functional Materials and Devices
Institute of Functional Nano and Soft Materials (FUNSOM)
Joint International Research Laboratory of Carbon-Based Functional Materials and Devices
Soochow University
199 Ren'ai Road, Suzhou, Jiangsu 215123, China
E-mail: vp293@suda.edu.cn
M. Liu, P. Vivo
Hybrid Solar Cells, Faculty of Engineering and Natural Sciences
Tampere University
P.O. Box 541, Tampere FI-33014, Finland

1. Introduction

Recent years have witnessed the exponential growth of the Internet of Things (IoT), which comprises an ultra-large ecosystem of sensor nodes that are being disseminated in everyday objects and environments to enhance our quality of life.[1–3] The IoT revolution has led to strong demand for easy-to-fabricate visible-light photodetectors that could be deployed ubiquitously—for example, to address applications in computer vision, smart homes, visible light communications, biomedicine, smart manufacturing, security, and environmental monitoring.[4–9] While silicon technologies have dominated the visible-light photodetector market to date,[10] they involve complex, energy-intensive fabrication processes and a capital-intensive fabrication infrastructure.[11,12] Therefore, for ubiquitous light sensing to become possible, it is essential to develop photodetector technologies based on thin-film photoactive materials that can be deposited through facile, low-cost, solution-based methods.[7,8,13,14] Crucially, for the development of the IoT ecosystem to be sustainable, its sensor nodes should function with ultra-low power consumption so as to operate autonomously and perpetually (e.g., without a connection to the grid or the need to frequently replace or recharge batteries).[15,16] To enable ubiquitous and energy-neutral light sensing for the IoT revolution, it is therefore highly desirable to develop photodetector technologies that are based on solution-processed photoactive materials and that can operate with no power consumption (i.e., in self-powered mode).

Among the solution-processable photoactive materials being investigated for optoelectronic applications, halide perovskites have risen to prominence in recent years due to their remarkable optoelectronic properties and facile processing.[17,18] While the bulk of perovskite research has focused on photovoltaics,[19,20] halide perovskites have also garnered a considerable amount of attention for photodetection,[21,22] including in self-powered mode.[23–25] However, mainstream halide perovskites contain lead, which is inherently toxic,[26] and have also faced important stability issues.[27,28] This has prompted the scientific community to search for lead-free perovskite-inspired materials

(PIMs), targeting safer compositions (conducive to reduced toxicity and environmental impacts) while also aiming to replicate the structural and electronic properties of lead-halide perovskites.[29,30] In particular, PIMs based on antimony and bismuth have come to the fore as particularly attractive. In addition to the lower toxicity of Sb and Bi compared to Pb,[15] the appeal of antimony- and bismuth-based PIMs is due to the similarity of the Sb^{3+} and Bi^{3+} cations to the Pb^{2+} found in the lead-halide perovskites in terms of size, polarizability, and valence shell,[29] which has enabled the resultant lead-free PIMs to reproduce key attractive electronic features of the lead-halide perovskites.[31]

Due to the 3+ oxidation state of their cations, antimony and bismuth deliver halide PIMs with reduced dimensionality. Absorbers that have captured a considerable amount of attention include compounds with a general formula $A_3M_2X_9$ (A^+: monovalent cation; M^{3+}: Sb^{3+} or Bi^{3+}; X^-: halide anion). These absorbers may have 0D lattices featuring isolated $[M_2X_9]^{3-}$ bi-octahedra, or 2D lattices comprising sheets of staggered, corner-sharing $[MX_6]^{3-}$ octahedra.[29,32] It is worth noting that many $A_3M_2X_9$ materials absorb through the visible range,[33–36] which makes them potentially suitable for visible-light detection. Other antimony- and bismuth-based PIMs whose absorption range covers the visible spectrum include $CsBi_3I_{10}$, whose structural dimensionality is intermediate between 0D and 2D (0D/2D),[37] as well as 1D materials featuring chains of corner-sharing $[MX_6]^{3-}$ octahedra separated by organic cations.[38,39]

While 2D $A_3Sb_2X_9$ compounds feature the highest dimensionality among all the antimony-based PIMs, only lower-dimensional (<2D) antimony-based PIMs have thus far been investigated for visible-light photodetection.[38,40] This reflects the fact that research on 2D $A_3M_2X_9$ absorbers is still in its nascent stage, since low-temperature, solution-based strategies to deposit such materials have only been demonstrated recently.[35,41] Indeed, the general focus on 0D $A_3M_2X_9$ absorbers can be traced to the fact that typical $A_3M_2X_9$ compositions and processing conditions for visible-light photodetection lead to a 0D structure.[29,42,43] Moreover, while the adoption of $X^- = Br^-$ or Cl^- allows the formation of a 2D structure, the corresponding bandgap is too large for visible-light detection.[40,44–48] More generally, the external quantum efficiencies (EQEs) of $A_3M_2X_9$ photodetectors operated in self-powered mode have been rather modest, typically in the range of ≈0.5–5% (i.e., much lower compared to lead-halide perovskite photodetectors).[48–50] 0D/2D bismuth-based PIMs have also delivered comparatively low EQEs in self-powered mode.[51,52] Therefore, it is not surprising that most photodetector studies to date featuring antimony- and bismuth-based PIMs have resorted to operation with an applied bias voltage,[38–40,44–47,53–58] as that can generally mitigate the effects of an inefficient photoconversion process.

In addition to a large photoconversion efficiency, real-world applications require photodetectors to deliver a photoresponse that is linear with optical power. Interestingly, most photodetectors comprising antimony- and bismuth-based PIMs have revealed a strongly sublinear photoresponse to date,[38–40,46,49–57,59] which suggests the presence of broad, non-uniform distributions of defect levels within the forbidden gap.[60–62] Among the very few implementations exhibiting a linear behavior, those operated in self-power mode could maintain their linearity over

an optical power range narrower than three orders of magnitude (i.e., appreciably narrower than lead-halide perovskite photodetectors).[25,48]

Aiming for the realization of the full potential of lead-free PIMs for easy-to-fabricate, self-powered, visible-light photodetectors, in this study we investigate, for the first time, the impact of the structural dimensionality of antimony-based perovskite-inspired absorbers on their self-powered photodetection capabilities. Capitalizing on the ability to deposit high-quality layers of 2D $Rb_3Sb_2I_9$ and to control the dimensionality (0D vs 2D) of the $Cs_3Sb_2X_9$ system via halide mixing, we carry out a comparative assessment of the performance of self-powered photodetectors based on 2D and 0D absorbers (i.e., 2D $Rb_3Sb_2I_9$ and 2D $Cs_3Sb_2I_{9-x}Cl_x$ versus 0D $Cs_3Sb_2I_9$). Specifically, we examine in detail their photoconversion efficiencies, photocurrent-power relationships, and speed of response. Based on detailed structural and optoelectronic characterization, we additionally provide physical insight into the observed trends in photodetector performance. This study thus brings to the fore that the control of the structural dimensionality of lead-free antimony-based absorbers offers a promising perovskite-inspired route to next-generation, self-powered photodetectors.

2. Results and Discussion

Given that the dimensionality of PIMs plays a central role in determining their optoelectronic properties (e.g., their charge transport properties[35,63–65]), we conjectured that 2D antimony-based $A_3M_2X_9$ compounds could potentially enable higher photodetector performance than the lower-dimensional counterparts explored to date. Therefore, to investigate the impact of dimensionality on the performance of self-powered lead-free PIM photodetectors, we focused on 2D $Cs_3Sb_2I_{9-x}Cl_x$ and $Rb_3Sb_2I_9$ as well as zero-dimensional $Cs_3Sb_2I_9$. While $Rb_3Sb_2I_9$ inherently forms a 2D structure featuring sheets of corner-sharing octahedra (**Figure 1**a),[36,66] $Cs_3Sb_2I_9$ comes in a 0D structure with isolated $[Sb_2I_9]^{3-}$ bi-octahedra (Figure 1a),[35,66,67] unless dedicated, high-temperature (≥230 °C) processing protocols are adopted.[63,68] However, we recently found that the fractional substitution of iodines with chlorines in $Cs_3Sb_2I_9$ (leading to $Cs_3Sb_2I_{9-x}Cl_x$) enables its conversion from a 0D to a 2D structure (Figure 1a) within a low-temperature, solution-based deposition process.[35] Specifically, we reported that the conversion of $Cs_3Sb_2I_{9-x}Cl_x$ to its 2D phase could be achieved with a nominal $x = 2$–4 (as per precursor mixing ratios) and that optimal solar cell performance could be achieved for nominal $x = 3$, which, in fact, corresponds to an actual x approaching 2 (as determined via energy dispersive X-ray spectroscopy).[35] Therefore, in the present study, we used $Cs_3Sb_2I_{9-x}Cl_x$ films with x approaching 2 (obtained with the precursor mixing ratios specified in the Experimental Section), which we shall refer to as $Cs_3Sb_2I_{9-x}Cl_x$ for the sake of simplicity.

In line with the overarching goal of developing easy-to-fabricate, solution-based photodetectors, we pursued the deposition of $Cs_3Sb_2I_9$, $Cs_3Sb_2I_{9-x}Cl_x$, and $Rb_3Sb_2I_9$ layers by spin-coating suitable precursors from common organic solvents (see the Experimental Section for details). Further, in line with our recent findings,[35,36] we adopted vapor-assisted annealing methods (see

2106295 (2 of 13)
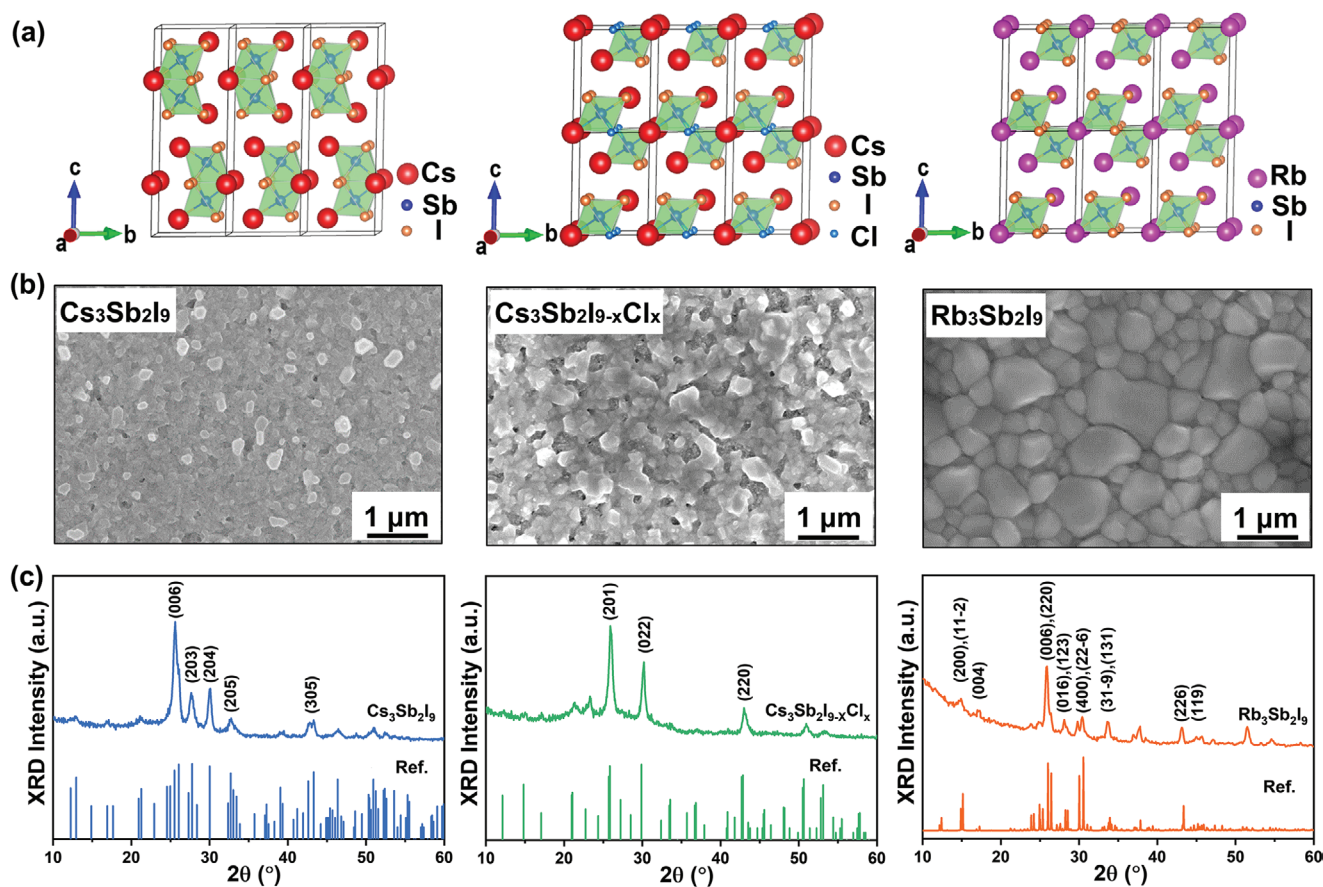
Figure 1. a) Crystal structures of 0D-$Cs_3Sb_2I_9$ (left), 2D-$Cs_3Sb_2I_{9-x}Cl_x$ (middle), and 2D-$Rb_3Sb_2I_9$ (right). b) Top-view SEM images of the resultant layers. Consistent with their optimal processing conditions for photodetector fabrication, 0D-$Cs_3Sb_2I_9$ and 2D-$Cs_3Sb_2I_{9-x}Cl_x$ were deposited on FTO/c-TiO_2/mp-TiO_2 substrates, while 2D-$Rb_3Sb_2I_9$ was deposited on FTO/c-TiO_2 substrates. c) Measured and reference XRD patterns (ICSD collection codes 001447 and 089695 for 0D- and 2D-$Cs_3Sb_2I_9$, respectively;[69] the reference pattern for 2D-$Rb_3Sb_2I_9$ was derived from ref. [66]).

the Experimental Section for details) to enhance the crystallinity and overall quality of the PIM layers. Following the indications from our photovoltaic studies on these PIMs,[35,36] we specifically adopted FTO/c-TiO_2/mp-TiO_2 substrates (FTO: fluorine-doped tin oxide; c-TiO_2: compact TiO_2; mp-TiO_2: mesoporous TiO_2) for the deposition of $Cs_3Sb_2I_{9-x}Cl_x$ and $Cs_3Sb_2I_9$ layers, while we resorted to FTO/c-TiO_2 substrates for $Rb_3Sb_2I_9$ (see below). The optimized process conditions delivered the layer morphologies shown in Figure 1b, as captured via scanning electronic microscopy (SEM). All layers appeared generally dense, with $Cs_3Sb_2I_{9-x}Cl_x$ and $Cs_3Sb_2I_9$, however, featuring sparse, minuscule pinholes. Additionally, the $Rb_3Sb_2I_9$ layers exhibited the largest domains (average lateral size of 629 nm), while the $Cs_3Sb_2I_{9-x}Cl_x$ and $Cs_3Sb_2I_9$ layers had average domain sizes of 435 and 209 nm, respectively (see also Figure S1, Supporting Information for the domain size distributions).

The structural identity and dimensionality of the different layers were confirmed via X-ray diffraction (XRD) (Figure 1c). The $Cs_3Sb_2I_9$ layers manifested a diffraction pattern consistent with its 0D phase (hexagonal, space group $P6_3/mmc$),[69,70] as made evident by the presence of the characteristic peaks at 27.7° and 32.7°. By contrast, the XRD pattern of the $Cs_3Sb_2I_{9-x}Cl_x$ samples closely followed the reference pattern of 2D $Cs_3Sb_2I_9$ (trigonal, space group $P\bar{3}m1$), confirming the conversion to a 2D structure through halide mixing.[69,71] In regard to the $Rb_3Sb_2I_9$

samples, they gave XRD patterns consistent with the expected 2D structure (monoclinic, space group $P2_1/n$).[66] Importantly, all peaks in the XRD patterns of the different PIM layers were consistent with the reference patterns, indicating the high purity of the layers. Having confirmed the structural dimensionality of our PIM layers, we shall now refer to the different PIMs as 0D-$Cs_3Sb_2I_9$, 2D-$Cs_3Sb_2I_{9-x}Cl_x$, and 2D-$Rb_3Sb_2I_9$ in the text for the sake of clarity. Finally, it is worth noting that the strongest XRD peak of the 2D-$Rb_3Sb_2I_9$ films was at 25.9°, which denotes a preferential crystalline orientation along the (006) planes, that is, with the sheets of corner-sharing octahedra parallel to the substrate surface. By contrast, the strongest XRD peaks of the 2D-$Cs_3Sb_2I_{9-x}Cl_x$ layers were at 25.9° and 29.9° (corresponding to the (201) and (022) planes, respectively) and had comparable intensity. Therefore, the 2D-$Cs_3Sb_2I_{9-x}Cl_x$ layers manifested a random orientation of their sheets of corner-sharing octahedra with respect to the substrate surface, which is advantageous (compared to a preferential in-plane orientation) for efficient charge collection in sandwich-type devices.[35,71]

We additionally characterized the optical absorption properties of the PIMs, given the generally close relationship between the optical absorption spectrum of a photoactive material and the resultant spectral responsivity in photodetectors. To correct for the reflection and scattering losses inherently present in spectrophotometry measurements on thin films, we
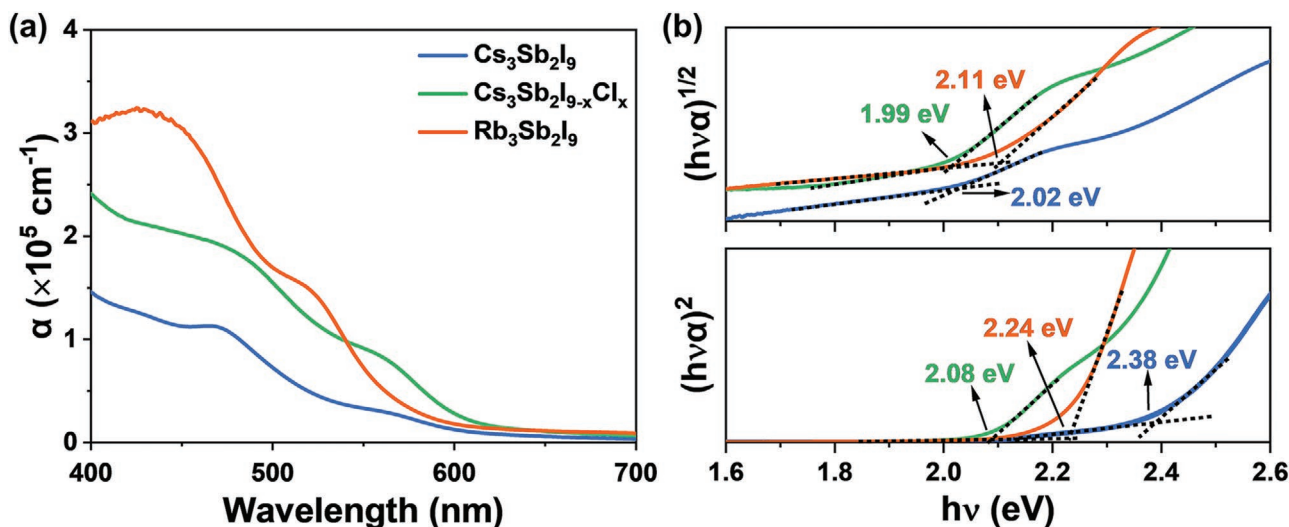
Figure 2. a) Absorption coefficients and b) Tauc plots of the PIM films deposited on glass substrates.

determined the absorption coefficient as $\alpha = \ln[(1 - R)/T]/t$. Here, R and T are the reflectance and transmittance, respectively, of the PIM thin films on glass, while t is their thickness. As shown in **Figure 2**a, the 2D PIMs (i.e., 2D-$Cs_3Sb_2I_{9-x}Cl_x$ and 2D-$Rb_3Sb_2I_9$) delivered high absorption coefficients in the $2–3 \cdot 10^5$ cm^{-1} range, with apparent onsets around 600 nm, pointing to their potential as thin-film absorbers for visible-light detection.[8,21] While having a similar onset, the absorption coefficient of 0D-$Cs_3Sb_2I_9$ was lower and manifested a much shallower rise below the onset. These findings are consistent with the quasi-direct nature of the optical gap of 2D-$Cs_3Sb_2I_{9-x}Cl_x$, given that its indirect and direct transitions (at 1.99 and 2.08 eV, respectively) were within ≈90 meV from each other, as we determined through Tauc analysis (Figure 2b). In contrast, the Tauc plots of 0D-$Cs_3Sb_2I_9$ revealed the indirect nature of its optical gap, which amounted to 2.02 eV (cf. its direct transition was at 2.38 eV; Figure 2b), in good agreement with the literature.[35,72] Finally, the 2D-$Rb_3Sb_2I_9$ films provided a somewhat intermediate case: they presented an indirect optical gap (=2.11 eV) but their direct transition (at 2.24 eV) was comparatively closer than in the 0D-$Cs_3Sb_2I_9$ case (see also Table S1, Supporting Information for a summary of the optical gaps of the PIMs).

Additional insight into the optical properties of the PIMs was gained from their steady-state photoluminescence (PL) spectra and time-resolved PL (TRPL) decays. **Figure 3**a–c shows the room-temperature (RT) PL spectra of the different PIMs (excitation photon energy $h\nu = 2.65$ eV). 0D-$Cs_3Sb_2I_9$ exhibited a broad emission band centered at ≈1.55 eV (Figure 3a), indicating a remarkably large Stokes shift of 0.47 eV. Such a broad PL band at energies <1.75 eV was also reported for 0D-$Cs_3Sb_2I_9$ at low temperatures (<200 K)[65] and for the analogous 0D-$Cs_3Bi_2I_9$ at RT.[73] It is known that a strong electron-phonon coupling effect is responsible for the broadness of the emission bands of similar PIMs,[74] inducing small polarons that restrain the charge carriers and leading to the formation of self-trapped excitons (STE) upon photoexcitation. Compared to the 2D counterparts, the 0D structure of 0D-$Cs_3Sb_2I_9$ may lead to stronger self-trapping, since it may facilitate the capture of charge carriers by

the Cs^+ cations and $[Sb_2I_9]^{3-}$ anions. By contrast, asymmetric emission bands were observed from both 2D-$Cs_3Sb_2I_{9-x}Cl_x$ and 2D-$Rb_3Sb_2I_9$, with maxima at 1.95 and 1.87 eV, respectively (Figure 3b,c). Multiple emission peaks are expected to contribute to the asymmetry of the observed emission bands. Therefore, we deconvolved the PL spectra of 2D-$Cs_3Sb_2I_{9-x}Cl_x$ and 2D-$Rb_3Sb_2I_9$ into three Gaussian bands each (Figure 3b,c). The three emission peaks at 1.97, 1.83, and 1.56 eV associated with the PL spectrum of 2D-$Cs_3Sb_2I_{9-x}Cl_x$ can be assigned to band edge emission (direct transition), STE emission, and defect-assisted emission,[75] respectively. The band edge emission (peak energy = 1.97 eV) dominates the PL spectrum, as it provides the main contribution to the PL peak at 1.95 eV. This is in good agreement with the determined quasi-direct nature of the optical gap of 2D-$Cs_3Sb_2I_{9-x}Cl_x$. On the other hand, for 2D-$Rb_3Sb_2I_9$, the Gaussian bands centered at 2.00, 1.85, and 1.60 eV can be assigned to phonon-assisted recombination of indirect excitons, STE emission (dominant pathway), and defect-assisted emission, respectively. The proposed recombination pathways for excitons in the different PIMs are depicted in Figure 3d.

The excited-state dynamics were revealed by recording TRPL decays monitored at their respective PL peaks, as shown in Figure 3e. All decays could be well fitted with a bi-exponential function (see Table S2, Supporting Information for a summary of the fitting parameters). To compare the timescales of the different decays, we also calculated the effective lifetime $\tau_{1/e}$, defined as the time after the initial excitation at which the PL intensity I_{PL} was reduced by a factor of e (i.e., $I_{PL}(\tau_{1/e}) = I_{PL}(0)/e$). The PL decay of 0D-$Cs_3Sb_2I_9$ exhibited the shortest effective lifetime ($\tau_{1/e} = 0.32$ ns), as STE-induced non-radiative recombination is the dominant process. The 2D-$Cs_3Sb_2I_{9-x}Cl_x$ samples exhibited the longest $\tau_{1/e}$ (1.62 ns), while a $\tau_{1/e}$ of 0.93 ns was achieved for 2D-$Rb_3Sb_2I_9$. This suggests that the 2D structure favors the extension of the excited-state lifetime compared to the 0D structure, due to the effective generation of free excitons and the reduced formation of STE. Further, while being comparable to that of the 2D-$Cs_3Sb_2I_{9-x}Cl_x$ samples, the lower
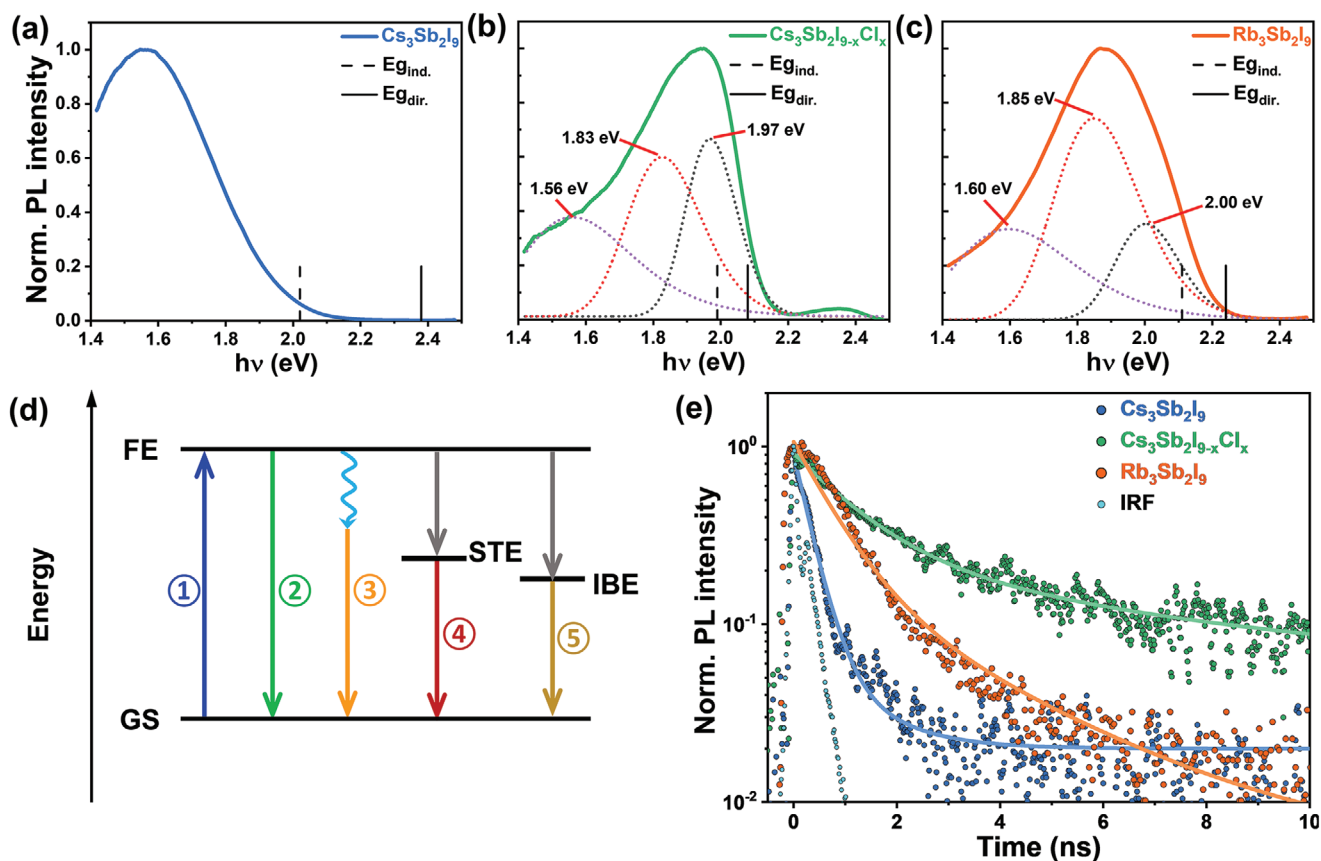
**Figure 3.** Steady-state room-temperature PL spectra of a) 0D-$Cs_3Sb_2I_9$, b) 2D-$Cs_3Sb_2I_{9-x}Cl_x$, and c) 2D-$Rb_3Sb_2I_9$. Deconvolved band representations of the emission from 2D-$Cs_3Sb_2I_{9-x}Cl_x$ and 2D-$Rb_3Sb_2I_9$ are also displayed in (b) and (c), respectively. d) Proposed recombination pathways. FE: free exciton; GS: ground state; IBE: impurity-bound exciton; STE: self-trapped exciton; ①: photo-excitation; ②: direct transition; ③: phonon-assisted indirect transition; ④: STE emission; ⑤: defect-assisted emission. Recombination pathways assignment: 1) 0D-$Cs_3Sb_2I_9$: ④; 2) 2D-$Cs_3Sb_2I_{9-x}Cl_x$: ②,④,⑤; 3) 2D-$Rb_3Sb_2I_9$: ③,④,⑤. e) TRPL decays of 0D-$Cs_3Sb_2I_9$, 2D-$Cs_3Sb_2I_{9-x}Cl_x$, and 2D-$Rb_3Sb_2I_9$, excited at 483 nm (excitation intensity ≈ 15 nJ cm^{-2}). The solid lines represent the fits to a bi-exponential function of the type $I_{PL}(t) = A_1 \exp(-t/\tau_1) + A_2 \exp(-t/\tau_2)$. IRF represents the instrument response file.

effective lifetime of the 2D-$Rb_3Sb_2I_9$ layers is indicative of the slightly higher capture rate associated with their non-radiative recombination centers, as per Shockley–Read–Hall recombination.[76] Therefore, the observed difference in effective lifetimes between the two 2D PIMs studied herein may be due to the fact that the defect levels involved in non-radiative recombination in 2D-$Rb_3Sb_2I_9$ have higher volumetric densities and/or larger capture cross sections.

To assess the capability of the PIMs for self-powered photodetection, we embedded them in devices featuring the n-i-p sandwich-type device architecture shown in **Figure 4**a. Specifically, we used FTO/TiO$_2$ as the cathode assembly and Au/poly-TPD as the anode assembly. This particular choice of electrodes and charge transport layers was based on energy level considerations. On the one hand, given the limited (built-in) electric field available in self-powered operation, it is crucial to ensure a sufficiently large driving force for photocarrier extraction in the form of favorable energy steps at the interfaces between the photoactive material and the charge transport layers.[77,78] On the other hand, the charge transport layers should have sufficiently large bandgaps in order to provide a barrier to dark carrier injection, which would negatively impact the noise performance of the photodetectors. TiO$_2$ and poly-TPD would

meet these requirements, in consideration of their energy levels as well as those of the PIMs considered herein (Figure 4b).[35,36] In regard to the electron transport layer, we adopted a compact TiO$_2$ (c-TiO$_2$) layer in the $Rb_3Sb_2I_9$ devices due to the optimal morphology of the 2D-$Rb_3Sb_2I_9$ films on such a layer.[36] In contrast, we resorted to a mesoporous TiO$_2$ (mp-TiO$_2$) layer atop a c-TiO$_2$ layer for the fabrication of 2D-$Cs_3Sb_2I_{9-x}Cl_x$ and 0D-$Cs_3Sb_2I_9$ devices as a means of boosting their photoconversion efficiency, given the smaller domain size of the 2D-$Cs_3Sb_2I_{9-x}Cl_x$ and 0D-$Cs_3Sb_2I_9$ layers.

To assess the capability of the aforementioned devices for self-powered photodetection, we first characterized their EQE spectra (Figure 4c) while the devices were biased with 0 V across. The EQE was determined as EQE(λ) = $(J_{ph}(\lambda)/q)/(P_{opt}(\lambda)/h\nu)$, where J_{ph} is the photocurrent density, P_{opt} is the incident optical power per unit area, q is the elementary charge, h is Planck's constant, and ν is the photon frequency. All the devices gave a broadband photoresponse in line with their absorption spectra, spanning the visible range up to wavelengths of ≈600 nm (Figure 4c). Specifically, the 2D-$Cs_3Sb_2I_{9-x}Cl_x$ devices covered the widest spectral range, consistent with the smaller and quasi-direct gap of 2D-$Cs_3Sb_2I_{9-x}Cl_x$. In particular, if we define the EQE onset wavelength, $\lambda_{onset}^{(EQE)}$, as the longest
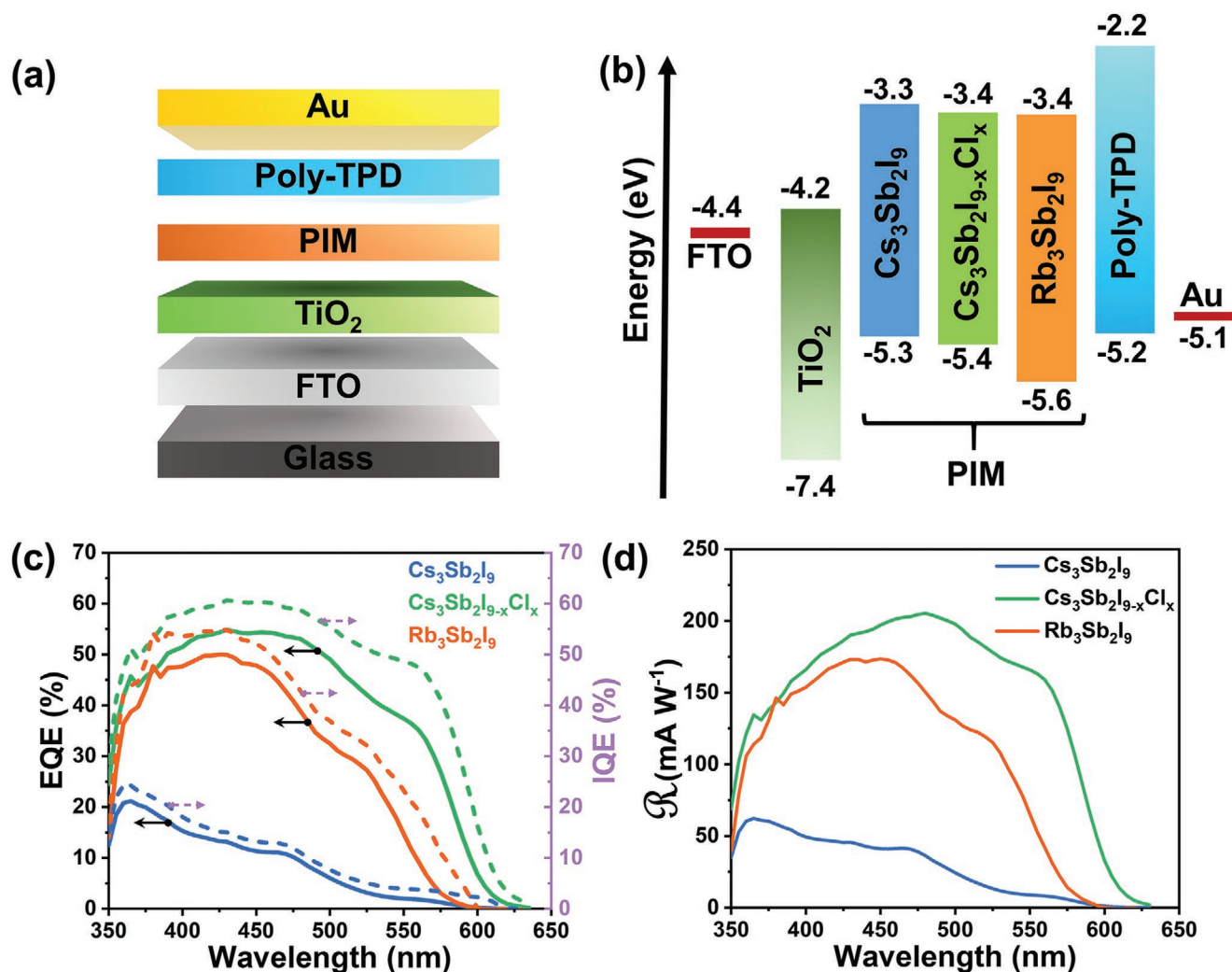
Figure 4. a) Schematic of the device stack of the PIM photodetectors. b) Corresponding energy-level diagram, based on the energy level values in refs. [35,36,79]. c) EQE and IQE spectra in self-powered mode. d) Corresponding spectral responsivities.

wavelength at which a photodetector achieves an EQE of 0.5%, we obtain $\lambda_{onset}^{(EQE)} = 628$ nm for the 2D-$Cs_3Sb_2I_{9-x}Cl_x$ devices, which reveals their suitability for near-infrared-blind visible-light detection.[62] Consistent with the trend associated with their optical gaps, the 2D-$Rb_3Sb_2I_9$ and 0D-$Cs_3Sb_2I_9$ photodetectors gave smaller $\lambda_{onset}^{(EQE)}$ values (593 and 591 nm, respectively). The EQE spectra of the 2D-$Cs_3Sb_2I_{9-x}Cl_x$ photodetectors also exhibited a considerably steeper EQE slope in the vicinity of the onset, adding to the benefits of the quasi-direct optical gap of 2D-$Cs_3Sb_2I_{9-x}Cl_x$.

Crucially, the EQE spectra revealed that the PIM photodetectors could function in self-powered mode. In particular, the devices based on 2D PIMs (i.e., 2D-$Cs_3Sb_2I_{9-x}Cl_x$ and 2D-$Rb_3Sb_2I_9$) exhibited considerably higher EQE values, with the 2D-$Cs_3Sb_2I_{9-x}Cl_x$ and 2D-$Rb_3Sb_2I_9$ devices reaching 55% and 50%, respectively. By contrast, the 0D-$Cs_3Sb_2I_9$ devices had appreciably lower EQE (up to 21%). This trend in the EQE values of the different PIMs was reproducibly observed (see Figure S2, Supporting Information). Importantly, the EQE values of our 2D-$Cs_3Sb_2I_{9-x}Cl_x$ and 2D-$Rb_3Sb_2I_9$ devices are

the highest reported to date for self-powered photodetectors based on solution-processed antimony- and bismuth-based absorbers,[48–52] with an improvement by more than a factor of ten compared to prior self-powered $A_3M_2X_9$ implementations (Table S3, Supporting Information).[48–50]

To gain insight into the intrinsic ability of the different PIMs to deliver efficient photoconversion in self-powered mode, we determined the internal quantum efficiency (IQE) of their photodetectors. Indeed, the IQE quantifies the number of photogenerated electron–hole pairs collected per absorbed photon (hence aggregating the photogeneration efficiency, η_{gen}; the efficiency of photocarrier transport through the photoactive material, η_{tr}; and the efficiency of photocarrier collection at the interface with the electrode assemblies, η_c).[7,80] Specifically, we determined the IQE as $IQE = EQE/(1 - R - T)$, where R and T are the reflectance and transmittance, respectively, of the corresponding device stacks.[66,81,82] The resultant IQE spectra (Figure 4c) first revealed that the efficiency losses (i.e., IQE − EQE) associated with light in-coupling amounted to 3–15% for all photodetectors. This implies that improved light

**ADVANCED
SCIENCE NEWS**

www.advancedsciencenews.com

**ADVANCED
FUNCTIONAL
MATERIALS**

www.afm-journal.de

management (e.g., antireflective coatings at the input interface and nanophotonic structures at the anode) could be pursued in the future to further increase the EQE. Moreover, the IQE spectra confirmed the superior intrinsic photoconversion efficiency of the 2D PIMs in comparison to the 0D counterpart: while the 2D-$Cs_3Sb_2I_{9-x}Cl_x$ and 2D-$Rb_3Sb_2I_9$ devices delivered peak IQE values in the range of 55–61%, the 0D-$Cs_3Sb_2I_9$ devices were at below 25%.

The superior IQE of the 2D PIMs can be rationalized in terms of their reduced recombination losses compared to the 0D counterpart. On the one hand, the lower exciton-trapping energies of the 2D absorbers (see the steady-state PL data above) would be conducive to a higher photogeneration efficiency (i.e., number of photogenerated carriers per absorbed photon). Similarly, the improved IQE of the 2D-$Cs_3Sb_2I_{9-x}Cl_x$ devices compared to the 2D-$Rb_3Sb_2I_9$ counterparts may also originate from the smaller impact of STE in 2D-$Cs_3Sb_2I_{9-x}Cl_x$ compared to 2D-$Rb_3Sb_2I_9$ (see the steady-state PL data above). On the other hand, drawing from Crandall's photocurrent model,[83–85] the superior IQE of the 2D-$Cs_3Sb_2I_{9-x}Cl_x$ devices would also benefit from their reduced non-geminate recombination losses (i.e., higher η_{tr}), as suggested by the longer carrier lifetime (see above) and larger mobility (as detailed in our recent report[35]) of 2D-$Cs_3Sb_2I_{9-x}Cl_x$ compared to 0D-$Cs_3Sb_2I_9$. Along similar lines, the relative magnitude of the IQE of the 2D-$Rb_3Sb_2I_9$ devices compared to the 2D-$Cs_3Sb_2I_{9-x}Cl_x$ and 0D-$Cs_3Sb_2I_9$ counterparts may also be contributed by the differences in carrier lifetimes, consistent with our TRPL findings (see above). Overall, the considerably higher photoconversion efficiencies of the 2D-$Cs_3Sb_2I_{9-x}Cl_x$ and 2D-$Rb_3Sb_2I_9$ photodetectors derive from the superior optoelectronic properties of the respective PIMs enabled by their higher dimensionality.

Interestingly, the IQE spectra of the 2D-$Cs_3Sb_2I_{9-x}Cl_x$ devices manifested a broad plateau region extending nearly over the entire absorption range, which is attractive for photodetector applications because it is conducive to an equalized spectral photoresponse. By contrast, the other PIMs exhibited a shallower rise to their IQE peaks as the wavelength was reduced below the absorption onset (see also Figure S3, Supporting Information). This suggests that photogeneration in 2D-$Cs_3Sb_2I_{9-x}Cl_x$ required lower excess energy than in 0D-$Cs_3Sb_2I_9$, which could reflect the reduced weight of dissipative processes during photogeneration (e.g., reduced self-trapping energy, as suggested by our PL findings). Similar considerations hold for the steeper IQE rise of the 2D-$Rb_3Sb_2I_9$ devices compared to the 0D-$Cs_3Sb_2I_9$ counterparts (Figure 4c; see also Figure S3, Supporting Information). Interestingly, 2D-$Cs_3Sb_2I_{9-x}Cl_x$ devices also present a steeper IQE rise compared to the 2D-$Rb_3Sb_2I_9$ counterparts, which may relate to the smaller role played by STE in 2D-$Cs_3Sb_2I_{9-x}Cl_x$ and its photoconversion efficiency. All of the above points to the significant impact of the photogeneration process on the IQE of the PIMs studied herein.

While the quantum efficiencies provide insight into the photoconversion process, photodetector applications critically depend on the magnitude of the photocurrent response per unit power, that is, the spectral responsivity $\mathcal{R} = J_{ph}(\lambda)/P_{opt}(\lambda)$. As shown in Figure 4d, the spectral responsivities of all PIM photodetectors follow the same trends as their EQE spectra, with only

minor red-shifts in their peak wavelengths. 2D-$Cs_3Sb_2I_{9-x}Cl_x$ and 2D-$Rb_3Sb_2I_9$ devices delivered peak responsivities of 205 and 174 mA W^{-1}, respectively, that is, 3–4 times larger than that of the 0D-$Cs_3Sb_2I_9$ devices (62 mA W^{-1}).

To gain further insight into the photoconversion process, we characterized the relationship between the photocurrent of the different self-powered photodetectors and the incident optical power. The significance of this relationship is due to the fact that, as a photodetector is subjected to increasing illumination levels, the hole and electron quasi-Fermi levels are swept closer to the valence and conduction bands, respectively. This allows the corresponding photocurrent to provide a probe into the dominant recombination mechanism and the energy landscape within the forbidden gap.[86,87] We thus illuminated the self-powered PIM photodetectors at $\lambda = 505$ nm (i.e., well within their responsivity range) with variable optical power densities within the range 10^{-3}–10^2 mW cm^{-2}. We found that the 2D PIMs delivered a photocurrent proportional to the incident optical power across the entire range probed (**Figure 5**). Specifically, when we fitted the corresponding datasets with the power law $J_{ph} \propto P_{opt}^{\theta}$, the resultant values of the exponent θ amounted to 0.98 and 0.99 for 2D-$Cs_3Sb_2I_{9-x}Cl_x$ and 2D-$Rb_3Sb_2I_9$, respectively, which are practically indistinguishable from unity, given the uncertainty limits of the experiment and the fitting routine. By contrast, the photocurrent-power traces associated with the 0D-$Cs_3Sb_2I_9$ devices only allowed piecewise power-law fits: on the one hand, for optical power densities below ≈20 μW cm^{-2} and above ≈100 μW cm^{-2}, the photocurrent was proportional to P_{opt} ($\theta = 1$); on the other hand, for intermediate power values, the photocurrent increased sublinearly ($\theta < 1$).

The observed J_{ph}–P_{opt} trends from all of the self-powered PIM devices can be rationalized in terms of the one-center model of the Rose–Bube theory, which involves non-radiative recombination through one single type of recombination centers (i.e., recombination centers with a given set of electron and hole capture cross sections) within the bandgap.[86,87] Specifically, the linear J_{ph}–P_{opt} relationship observed from the 2D PIM photodetectors (Figure 5) would arise from a discrete recombination center that lies deep within the forbidden gap, thereby remaining within the quasi-Fermi levels throughout the P_{opt} range probed. In other words, in the 2D PIM photodetectors, the quasi-Fermi levels would not cross such a recombination center, thus allowing the photosensitivity to remain constant ($\theta = 1$). By contrast, the behavior observed from the 0D-$Cs_3Sb_2I_9$ devices suggests the presence of recombination centers at two distinct energies within the forbidden gap. Specifically, while some centers would be located deep in the forbidden gap and would thus remain embraced within the quasi-Fermi levels throughout the P_{opt} range probed (as in the 2D PIM devices), a set of recombination centers lying closer to the band edges would be crossed by the quasi-Fermi levels as the optical power is raised, leading to a photosensitivity reduction. Indeed, Figure 5 reveals that the EQE of the 0D-$Cs_3Sb_2I_9$ devices at $\lambda = 505$ nm changes from ≈9% at low optical power (corresponding to the lower-lying segment with $\theta = 1$) to ≈3.5% at high optical power (corresponding to the higher-lying segments with $\theta = 1$).

The above J_{ph}–P_{opt} characterization additionally allowed us to assess the suitability of the self-powered PIM photodetectors for real-world applications in terms of photoresponse linearity. As
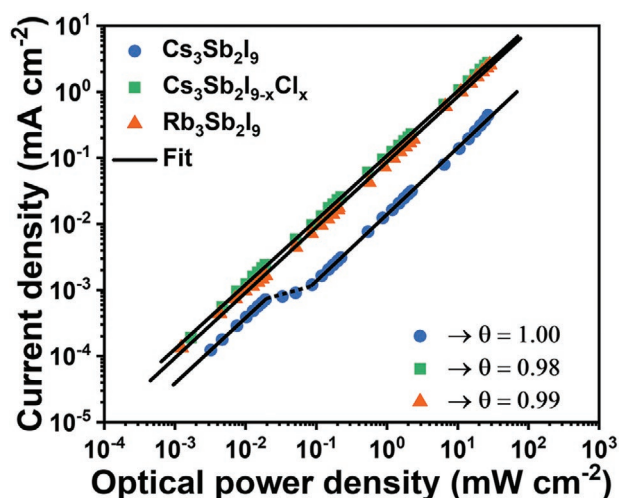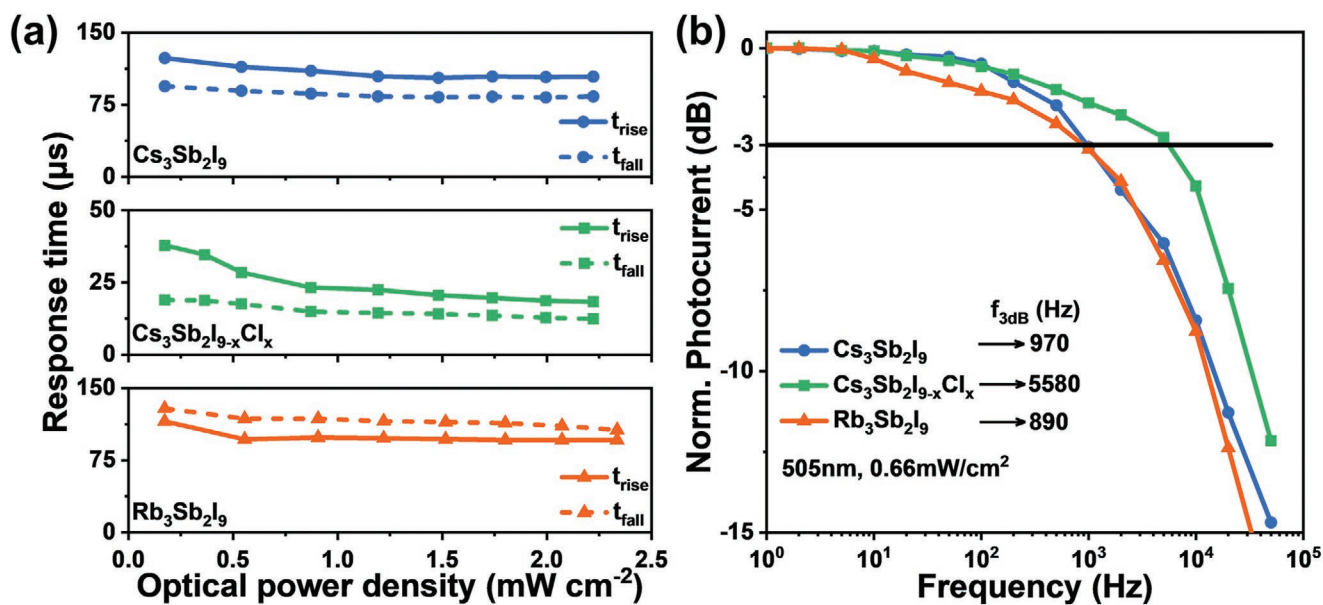
Figure 5. Photocurrent density, J_{ph}, of the PIM photodetectors measured at 0 V as a function of the incident optical power per unit area, P_{opt} (illumination at $\lambda = 505$ nm). The symbols represent the measured data points, while the overlaid segments denote the power-law fits of the type $J_{ph} = c\, P_{opt}^{\theta}$, where c and θ are fit parameters. The θ values associated with the fits are also provided (in the case of the 0D-$Cs_3Sb_2I_9$ devices, the θ value refers only to the linear segments of the corresponding curve).

noted earlier, both the 2D-$Cs_3Sb_2I_{9-x}Cl_x$ and 2D-$Rb_3Sb_2I_9$ photodetectors delivered a linear photoresponse over the entire optical power range probed (more than four orders of magnitude wide). Therefore, a lower bound on their linear dynamic range (LDR) could be determined as $LDR_U := 20\,log_{10}(J_{ph,max}^{(meas)}/J_{ph,min}^{(meas)})$, where $J_{ph,min}^{(meas)}$ and $J_{ph,max}^{(meas)}$ are the minimum and maximum measured photocurrents, respectively, over the probed P_{opt} range. We thus found that the LDR_U of both 2D-$Cs_3Sb_2I_{9-x}Cl_x$ and 2D-$Rb_3Sb_2I_9$ devices amounted to 83.3 dB. Importantly, given that the values of $J_{ph,min}^{(meas)}$ and $J_{ph,max}^{(meas)}$ used to calculate LDR_U were solely determined by the experimental limitations of our light sources and acquisition electronics, the resultant LDR_U values underestimate the actual LDR, which is defined as $LDR := 20\,log_{10}(J_{ph,max}/J_{ph,min})$, where $J_{ph,max}$ and $J_{ph,min}$ are the ultimate upper and lower bounds, respectively, of the linear region of operation. Nonetheless, the above LDR_U value is already well beyond (by more than 20 dB) the LDR of all reported self-powered photodetectors based on solution-based antimony- and bismuth-based PIMs (Table S3, Figure S4, Supporting Information).[48–52] Further, if one takes into account that the ultimate lower limit of the linear range of a photodetector is determined by its noise floor,[88] a more realistic estimate of the LDR of our photodetectors can be obtained by taking $J_{ph,min}$ as their noise currents (see below). In light of this, the LDR of the 2D-$Cs_3Sb_2I_{9-x}Cl_x$ and 2D-$Rb_3Sb_2I_9$ photodetectors would amount to at least 190 and 175 dB, respectively (see Figure S5, Supporting Information), which is competitive with benchmark photodetector technologies for the visible range.[7,89] Finally, given that the 0D-$Cs_3Sb_2I_9$ photodetectors were nonlinear over the entire optical power range probed, their LDR is not defined. This confirms the superior photodetector performance enabled by the higher dimensionality of the 2D $A_3Sb_2X_9$ PIMs.

Real-world applications also require photodetectors to be able to sense weak optical signals. To quantify such ability in our self-powered PIM photodetectors, we determined the specific detectivity D^*, which constitutes a normalized measure of the reciprocal of the minimum optical signal that can be detected. Specifically, we calculated the specific detectivity of our PIM photodetectors as $D^*(\lambda) = \mathcal{R}(\lambda)/(2\,q\,J_{d,0})^{1/2}$, taking into account the commonly adopted assumption of shot-noise-limited photodetection,[22,25,90] which therefore allows a direct comparison to the relevant literature. Here, $\mathcal{R}(\lambda)$ is the spectral responsivity, q is the elementary charge, and $J_{d,0}$ is the dark current density at 0 V (see Figure S6, Supporting Information). The resultant specific detectivity spectra are displayed in Figure S7, Supporting Information. All photodetectors gave maximum D^* values in the range of 10^{12} Jones. Importantly, the highest D^* (6.1×10^{12} Jones) was obtained from the 2D-$Cs_3Sb_2I_{9-x}Cl_x$ devices, while 0D-$Cs_3Sb_2I_9$ and 2D-$Rb_3Sb_2I_9$ gave D^* values of 3.5×10^{12} and 4.3×10^{12} Jones, respectively. The higher D^* of the 2D-$Cs_3Sb_2I_{9-x}Cl_x$ devices resulted from their having the highest responsivity (see above) as well as the lowest dark current density (256 pA cm^{-2}; see Figure S6, Supporting Information) among all of the PIM photodetectors considered herein. Importantly, the specific detectivity of the 2D-$Cs_3Sb_2I_{9-x}Cl_x$ devices is among the highest for self-powered antimony- and bismuth-based PIM photodetector[48–50,52] (see Table S3, Supporting Information) and is also competitive with self-powered photodetectors comprising lead-based perovskites.[25]

Given that real-world applications involve time-varying optical signals, self-powered photodetectors must respond sufficiently fast to acquire such signals.[7,76,91] Therefore, we characterized the speed of response of our photodetectors first by illuminating them with rectangular light pulses of variable optical power. In response, the self-powered PIM photodetectors delivered reproducible, quasi-rectangular photocurrent transients, in all cases reaching the steady state within the duration of the light pulses (Figures S8,S9, Supporting Information). We could thus quantify the speed of response of the photodetectors in terms of the rise time, t_{rise}, and the fall time, t_{fall}, required for their photocurrent transients to cover 50% of the full range on their rising and falling edges, respectively. As shown in **Figure 6**a, the 2D-$Cs_3Sb_2I_{9-x}Cl_x$ devices gave the highest speed of response, with an average response time, $t_r = (t_{rise} + t_{fall})/2$, down to 15 μs. Such a response time is more than six times shorter than that observed from the 0D-$Cs_3Sb_2I_9$ devices (t_r down to 94 μs), in line with the superior charge transport properties of 2D-$Cs_3Sb_2I_{9-x}Cl_x$.[35] In regard to the 2D-$Rb_3Sb_2I_9$ devices, they gave response times down to 101 μs, that is, comparable to the 0D-$Cs_3Sb_2I_9$ counterparts. This behavior can be linked to the planar device architecture of the 2D-$Rb_3Sb_2I_9$ devices, which results in carriers having to averagely travel a longer distance before reaching the electrodes compared to the mesoporous case. Regardless of the PIM and device architecture used, we observed a marginal reduction of the response times with the incident optical power, as well as a slight asymmetry between the fall and rise times. Both findings can be traced to trap-related effects. Indeed, on the one hand, trap-filling would have a reduced impact at higher carrier densities, thereby leading to a reduction of the response time with incident optical power. On the other hand, the different

Figure 6. a) Fall and rise times versus optical power density of the PIM photodetectors, as determined from their response to rectangular light pulses (Figure S8, Supporting Information). b) Normalized photocurrent amplitude acquired from the PIM photodetectors while they were subjected to a sinusoidally varying optical signal superimposed on a constant optical signal of 0.66 mW cm^{-2}. The resulting f_{3dB} values are also indicated in the plot. In both (a) and (b), a light-emitting diode (LED; $\lambda = 505$ nm) was used as the source.

balance between trap filling and emptying during the rising and falling edges of the photocurrent waveforms, as well as any spatial dependence thereof, would lead to asymmetric rise and fall times.[60,61,92] In particular, the 0D-Cs$_3$Sb$_2$I$_9$ and 2D-Cs$_3$Sb$_2$I$_{9-x}$Cl$_x$ gave fall times consistently shorter than the corresponding rise times (Figure 6a). This behavior may be traced to the greater impact of defect-level filling on the kinetics of the rising edges of the photocurrent response of such devices compared to that of defect-level emptying on their falling edges, given that the latter transients benefit from the fast decay rate of the free carrier population.[75] By contrast, the 2D-Rb$_3$Sb$_2$I$_9$ devices manifested rising edges that were faster compared to their falling edges. This behavior came along with a slight overshoot after light turn-on (Figure S8, Supporting Information), which has also been observed in other thin-film sandwich-type devices over the years.[93–95] Such an overshoot can be traced to a time-varying carrier trapping kinetics after light turn-on within the device stack, which involves a faster component leading to the initial overshoot prior to the slower component leading to the steady-state photocurrent.[93–95] By contrast, the falling edges of the photocurrent response of the 2D-Rb$_3$Sb$_2$I$_9$ devices take the form of monotonic decays, which can be thus traced solely to the emptying of defect levels,[93–95] thereby leading to longer fall times.

We additionally assessed the speed of response under sinusoidally modulated illumination of variable frequency (Figure 6b). In such a case, a useful metric to quantify the speed of response is the 3dB frequency f_{3dB}, at which the photocurrent amplitude is reduced by a factor of $\sqrt{2}$ compared to the amplitude under continuous illumination. The f_{3dB} values obtained from the self-powered 0D-Cs$_3$Sb$_2$I$_9$, 2D-Cs$_3$Sb$_2$I$_{9-x}$Cl$_x$, and 2D-Rb$_3$Sb$_2$I$_9$ photodetectors amounted to 970, 5580, and 890 Hz, respectively (Figure 6b). These f_{3dB} values reproduce

the same trend in the speed of response observed from the pulsed measurements, with the 2D-Cs$_3$Sb$_2$I$_{9-x}$Cl$_x$ devices being the fastest, followed by the 0D-Cs$_3$Sb$_2$I$_9$ and 2D-Rb$_3$Sb$_2$I$_9$ counterparts. Further, these f_{3dB} values are in good quantitative agreement with the response times t_r determined under pulsed illumination, as the first-order approximation of the 3dB frequency $f_{3dB}^{(0)} = \ln(2)/(2\pi t_r)$ as a function of the response time[7,96] delivers values within 20% of those experimentally determined. This confirms that the 2D-Cs$_3$Sb$_2$I$_{9-x}$Cl$_x$ photodetectors were superior to the 0D counterpart also in terms of speed of response. In fact, in spite of their operation in self-powered mode, the 3dB frequency of the 2D-Cs$_3$Sb$_2$I$_{9-x}$Cl$_x$ photodetectors was not only superior to that of all other photodetectors featuring solution-processed antimony- and bismuth-based A$_3$M$_2$X$_9$ PIMs in the literature,[40,44–50,53,56–58] but also at least an order of magnitude higher than all prior self-powered implementations.[48–50]

Finally, we assessed the stability of the different types of photodetectors by studying their photoresponse over a period of 600 h. Specifically, the devices were stored in an N$_2$-filled glove box during most of the stability experiment and were transferred to ambient air only at discrete intervals for characterization. During their characterization, the strength of the self-powered photocurrent response was measured while subjecting the photodetectors to pulsed illumination at $\lambda = 505$ nm. Importantly, the aforementioned storage conditions of the photodetectors in an N$_2$-filled glove box are comparable to those that would be obtained for encapsulated devices stored in ambient air.[97] In fact, the direct exposure of the non-encapsulated PIM devices to ambient air for several 1 h-long intervals during their characterization resulted in additional environmental stress. As can be seen from the dataset presented in Figure S10, Supporting Information, both types of photodetectors based on the 2D PIMs

**ADVANCED
SCIENCE NEWS**

www.advancedsciencenews.com

**ADVANCED
FUNCTIONAL
MATERIALS**

www.afm-journal.de

studied herein manifested considerably higher stability than the $0D$-$Cs_3Sb_2I_9$ photodetectors. On the one hand, the photocurrent response of the 2D-$Cs_3Sb_2I_{9-x}Cl_x$ devices was reduced by only 13% over 600 h, with the 2D-$Rb_3Sb_2I_9$ devices manifesting a similar trend (Figure S10, Supporting Information). On the other hand, the photocurrent response of the 0D-$Cs_3Sb_2I_9$ devices was reduced by 53% over the same amount of time (Figure S10, Supporting Information). The considerably higher stability of the photodetectors comprising the 2D antimony-based PIMs studied herein confirms their superiority over their 0D counterpart.

3. Conclusion

With the aim of advancing environmentally-friendly solutions for easy-to-fabricate self-powered photodetectors, herein we investigated, for the first time, the critical impact of the structural dimensionality of lead-free antimony-based PIMs on their self-powered photodetection capabilities. To provide a comparative assessment, we examined solution-processed photoactive layers made of 0D $Cs_3Sb_2I_9$ (0D-$Cs_3Sb_2I_9$) and 2D $Cs_3Sb_2I_{9-x}Cl_x$ and $Rb_3Sb_2I_9$ (2D-$Cs_3Sb_2I_{9-x}Cl_x$ and 2D-$Rb_3Sb_2I_9$). We thus revealed that photodetectors based on 2D $A_3Sb_2X_9$ absorbers—which had never been considered for self-powered photodetection to date—gave considerably higher self-powered photodetector performance compared to the 0D counterpart. In particular, the top performance was achieved with 2D-$Cs_3Sb_2I_{9-x}Cl_x$ photodetectors, which delivered record-high photoconversion efficiency, LDR, and speed of response compared to prior implementations of self-powered $A_3M_2X_9$ photodetectors: their EQE was up to 55%, that is, nearly three times higher than the corresponding 0D-$Cs_3Sb_2I_9$ devices and more than ten times higher than all prior self-powered $A_3M_2X_9$ implementations; their cutting-edge LDR extended over more than four orders of magnitude and potentially up to 190 dB; their 3dB frequency was >5 kHz, making our 2D-$Cs_3Sb_2I_{9-x}Cl_x$ photodetectors at least an order of magnitude faster than all prior implementations of self-powered $A_3M_2X_9$ photodetectors. Importantly, such performance levels are already sufficient to address self-powered photodetector applications such as in smart homes, smart manufacturing, wearables, and biomedicine.[62]

Furthermore, our study provided insight into the structure-property relations relevant to self-powered $A_3Sb_2X_9$ photodetectors based on detailed optoelectronic and device characterization. Specifically, we could trace the superiority of these 2D PIMs to their enhanced optoelectronic properties (e.g., longer carrier lifetimes and reduced impact of STE), as enabled by their higher dimensionality.

By delivering cutting-edge perovksite-inspired photodetector performance as well as insight into the relevant structure-property relations, our study provides both a technological opportunity and an essential material design rule for the future exploration of environmentally-friendly PIMs for high-performance self-powered photodetection.

4. Experimental Section

Materials: All commercially-sourced chemicals were employed as received and without additional purification: SbI_3 (99.999%, Sigma Aldrich), CsI (99.999%, Alfa Aesar), $SbCl_3$ (99.999%, Alfa Aesar), RbI (99.999%, Sigma Aldrich), dimethylsulfoxide (DMSO; analytical grade, Beijing Chemical Reagent Co.), *N,N*-dimethylfomamide (DMF; analytical grade, Beijing Chemical Reagent Co.), toluene (99.5%, Yonghua Chemistry), chlorobenzene (CB; > 99%, J&K), isopropyl alcohol (IPA; 99.5%, J&K), poly(4-butyl-*N,N*-diphenylaniline) (Poly-TPD; M_w = 6 000–20 000, Lumtec), titanium(IV) isopropoxide (97%, Sigma Aldrich), titania paste (18NR-T, Greatcell solar), acetone (> 99.5%, Jiangsu Qiangsheng functional Chemistry Co.), and ethanol (> 99.5%, Jiangsu Qiangsheng functional Chemistry Co.).

PIM Thin-Film Deposition: The PIM films were prepared in a glove box filled with ultra-high-purity nitrogen gas. 2D-$Cs_3Sb_2I_{9-x}Cl_x$ and 0D-$Cs_3Sb_2I_9$ films were prepared according to the procedure detailed in ref. [35]. Mixtures of the precursor powders (CsI:SbI_3 in a 3:2 mole ratio for 0D-$Cs_3Sb_2I_9$; CsI:SbI_3:SbCl_3 in a 3:1:1 mole ratio for 2D-$Cs_3Sb_2I_{9-x}Cl_x$) were dissolved in DMSO:DMF (3:1 volume ratio), targeting a solution concentration of 0.3 M. After being stirred and heated at 75 °C overnight, the solutions were filtered using PTFE filters with a 0.22 μm pore size. Thin films were then deposited by spin-coating 40 μL of the resulting solutions at 4000 rpm for 30 s. After fixed delays (15 and 20 s for 0D-$Cs_3Sb_2I_9$ and 2D-$Cs_3Sb_2I_{9-x}Cl_x$, respectively) from the start of the spin-coating cycles, 150 μL toluene was dispensed onto the spinning substrates. Finally, the resulting films were subjected to vapor-assisted annealing (on a hotplate at 105 and 150 °C for 0D-$Cs_3Sb_2I_9$ and 2D-$Cs_3Sb_2I_{9-x}Cl_x$, respectively) for 30 min, with the substrates and a 5 μL DMSO droplet in their vicinity placed within a Petri dish.

$Rb_3Sb_2I_9$ films were prepared as detailed in ref. [36]. A mixture of the precursor powders (RbI:SbI_3 in a mole ratio of 3:2) was dissolved in DMF, targeting a solution concentration of 0.25 M. After being stirred and heated at 75 °C overnight, the solutions were filtered using PTFE filters with a 0.22 μm pore size. Thin films were then deposited by spin-coating 40 μL of the resulting solution at 4000 rpm for 30 s. After 5 s from the start of the spin-coating cycle, 100 μL of an SbI_3 solution in toluene (10 g L^{-1}) was dispensed onto the spinning substrates. Finally, the samples were subjected to high-temperature vapor annealing in dry SbI_3 vapor, with the samples and 50 mg of SbI_3 powder placed inside a closed contained onto a hotplate. The annealing process consisted of the following sequence of steps: a) heating from room temperature to 225 °C for 10 min; 2) cooling down to 150 °C for 10 min; 3) heating at 150 °C for 10 min. Finally, the samples were taken out of the container and allowed to spontaneously cool down.

Device Fabrication: Glass substrates with pre-patterned FTO electrodes (Liaoning Youxuan New Energy Technology Co. Ltd.) were sequentially sonicated in an ultrasonic bath with deionized water, acetone, and ethanol (10 min each), after which they were blown dry with N_2 gas. The substrates to be used for the fabrication of 0D-$Cs_3Sb_2I_9$ and 2D-$Cs_3Sb_2I_{9-x}Cl_x$ devices were treated with UV-ozone (for 30 min), while those to be used for $Rb_3Sb_2I_9$ were treated with O_2 plasma (for 15 min). A compact TiO_2 (c-TiO_2) film was obtained by spin-coating a precursor solution of 5.06 mL 2-propanol, 380 μL titanium(IV) isopropoxide, and 35 μL dilute HCl (as reported in ref. [98]) at 4000 rpm for 30 s, followed by sintering at 450 °C for 40 min in air. Samples later used for the fabrication of 0D-$Cs_3Sb_2I_9$ and 2D-$Cs_3Sb_2I_{9-x}Cl_x$ devices were then coated with a layer of mesoporous TiO_2 (mp-TiO_2), which was obtained by spin-coating 18NR-T titania paste (0.2 g mL^{-1} in ethanol) at 7000 rpm for 30 s, followed by sintering at 450 °C for 40 min in air. Subsequently, the desired PIM layer was deposited as detailed in PIM Thin-Film Deposition section, followed by the spin coating of 40 μL poly-TPD solution (10 g L^{-1} in CB) at 4000 rpm for 30 s. Finally, 40-nm-thick Au electrodes were thermally evaporated through a shadow mask, defining a device active area of 7.25 mm².

Materials Characterization: XRD patterns were acquired using a Panalytical Emyrean X-ray diffractometer in air (λ = 1.5406 Å, tube current = 40 mA, generator voltage = 40 kV). Top-view SEM images of PIM films deposited on glass/TiO_2 were acquired using a Zeiss GeminiSEM 500 (accelerating voltage = 10 kV, pressure = 2 × 10^{-5} mbar). Reflectance and transmittance spectra were measured within an integrating sphere employing a PerkinElmer Lambda 950 UV–vis–NIR spectrophotometer.

The thickness of compact PIM films was measured with a profilometer (D-100 Stylus, KLA-Tencor). Steady-state PL spectra were collected with a FLS1000 spectrofluorometer (Edinburgh Instruments, UK). The TRPL decays were measured with a time-correlated single photon counting apparatus equipped with a Picoharp 300 controller and a PDL 800-B driver for excitation and a Hamamatsu R3809U-50 microchannel plate photomultiplier for detection in a 90° configuration.

Optoelectronic Characterization: EQE measurements were carried out in air using a customized setup comprising a source meter (Keithley 6420), a monochromated light source (Zolix, Omni-λ2005i), and a calibrated power meter assembly (Thorlabs PM200 and Thorlabs S120VC). Transient photocurrent measurements under variable-power illumination were carried out with an LED emitting at $\lambda = 505$ nm (LV CK7P-JYKZ-25, OSRAM Opto Semiconductors). The LED was driven with a pulsed current of variable magnitude supplied by a custom-built electronic module. The resultant photocurrent pulses from the PIM photodetectors were amplified with a DHPCA-100 signal amplifier (FEMTO). Sinusoidally-modulated photocurrent measurements were carried out in the same fashion but using a signal generator (PicoScope 5444B, Pico Technology) and a different custom-built electronic module to drive the LED source with a sinusoidally modulated current.

Stability Characterization: The stability of the non-encapsulated PIM photodetectors was studied over a period of 600 h. During most of this time, the devices were stored in an N_2-filled glove box. At discrete times (as indicated in Figure S10, Supporting Information), the devices were transferred to ambient air and their self-powered photocurrent response was measured while the photodetectors were subjected to pulsed illumination at $\lambda = 505$ nm (see Optoelectronic Characterization above) and with $P_{opt} = 1.21$ mW cm^{-2}. The non-encapsulated devices were kept in air during their characterization (requiring ≈1 h each time).

Supporting Information

Supporting Information is available from the Wiley Online Library or from the author.

Conflict of Interest

The authors declare no conflict of interest.

Data Availability Statement

The data that support the findings of this study are available from the corresponding author upon reasonable request.

[1] V. Pecunia, M. Fattori, S. Abdinia, H. Sirringhaus, E. Cantatore, *Organic and Amorphous-Metal-Oxide Flexible Analogue Electronics*, Cambridge University Press, Cambridge, UK **2018**.

[2] *Internet of Things A to Z*, (Ed: Q. Hassan), John Wiley & Sons, Inc., Hoboken, NJ, USA **2018**.

[3] A. Keshavarzi, W. van den Hoek, *IEEE Des. Test* **2019**, *36*, 41.

[4] P. C. Y. Chow, T. Someya, *Adv. Mater.* **2020**, *32*, 1902045.

[5] N. Strobel, N. Droseros, W. Köntges, M. Seiberlich, M. Pietsch, S. Schlisske, F. Lindheimer, R. R. Schröder, U. Lemmer, M. Pfannmöller, N. Banerji, G. Hernandez-Sosa, *Adv. Mater.* **2020**, *32*, 1908258.

[6] J. Oliveira, R. Brito-Pereira, B. F. Gonçalves, I. Etxebarria, S. Lanceros-Mendez, *Org. Electron.* **2019**, *66*, 216.

[7] V. Pecunia, *Organic Narrowband Photodetectors: Materials, Devices and Applications*, IOP Publishing, Bristol, UK **2019**.

[8] F. P. García de Arquer, A. Armin, P. Meredith, E. H. Sargent, *Nat. Rev. Mater.* **2017**, *2*, 16100.

[9] T. Lu, L. Huang, Y. Lee, K.-J. Tsai, Y. Liao, N. Cheng, Y. Chu, Y. Tsai, F. Chen, T. Chiueh, in *Proc. 53rd Annual Design Automation Conf.*, ACM, New York, NY, USA **2016**, pp. 1–5.

[10] Photodiode Sensors Market, https://www.transparencymarketresearch.com/photodiode-sensor-market.html (accessed: June 2021).

[11] M. Jamal Deen, P. K. Basu, *Silicon Photonics:Fundamentals and Devices*, John Wiley & Sons, Ltd, Chichester, UK **2012**.

[12] A. Rahim, T. Spuesens, R. Baets, W. Bogaerts, *Proc. IEEE* **2018**, *106*, 2313.

[13] D. Natali, M. Caironi, in *Photodetectors: Materials, Devices and Applications*, Elsevier, Cambridge, UK **2016**, p. 195–254.

[14] G. Konstantatos, E. H. Sargent, *Colloidal Quantum Dot Optoelectronics and Photovoltaics*, (Eds: G. Konstantatos, E. H. Sargent), Cambridge University Press, Cambridge, UK **2013**.

[15] V. Pecunia, L. G. Occhipinti, R. L. Z. Hoye, *Adv. Energy Mater.* **2021**, *11*, 2100698.

[16] P. Harrop, *Battery Elimination in Electronics and Electrical Engineering 2018–2028*, IDTechEx, Cambridge, UK **2017**.

[17] T. M. Brenner, D. A. Egger, L. Kronik, G. Hodes, D. Cahen, *Nat. Rev. Mater.* **2016**, *1*, 15007.

[18] Y. Chen, H. T. Yi, X. Wu, R. Haroldson, Y. N. Gartstein, Y. I. Rodionov, K. S. Tikhonov, A. Zakhidov, X. Y. Zhu, V. Podzorov, *Nat. Commun.* **2016**, *7*, 12253.

[19] A. K. Jena, A. Kulkarni, T. Miyasaka, *Chem. Rev.* **2019**, *119*, 3036.

[20] J. Y. Kim, J. W. Lee, H. S. Jung, H. Shin, N. G. Park, *Chem. Rev.* **2020**, *120*, 7867.

[21] V. Pecunia, *J. Phys.: Mater.* **2019**, *2*, 042001.

[22] M. Ahmadi, T. Wu, B. Hu, *Adv. Mater.* **2017**, *29*, 1605242.

[23] S. V. N. Pammi, V. Tran, R. Maddaka, J. Eom, J. S. Jung, H. Jeong, M. Kim, V. Pecunia, S. G. Yoon, *Adv. Opt. Mater.* **2020**, *8*, 2000845.

[24] S. V. N. Pammi, R. Maddaka, V. D. Tran, J. H. Eom, V. Pecunia, S. Majumder, M. D. Kim, S. G. Yoon, *Nano Energy* **2020**, *74*, 104872.

[25] C. Perumal Veeramalai, S. Feng, X. Zhang, S. V. N. Pammi, V. Pecunia, C. Li, *Photonics Res.* **2021**, *9*, 968.

[26] J. Li, H. Cao, W. Jiao, Q. Wang, M. Wei, I. Cantone, J. Lü, A. Abate, *Nat. Commun.* **2020**, *11*, 310.

[27] J. A. McLeod, L. Liu, *J. Phys. Chem. Lett.* **2018**, *9*, 2411.

[28] G. Divitini, S. Cacovich, F. Matteocci, L. Cinà, A. Di Carlo, C. Ducati, *Nat. Energy* **2016**, *1*, 15012.

[29] V. Pecunia, L. G. Occhipinti, A. Chakraborty, Y. Pan, Y. Peng, *APL Mater.* **2020**, *8*, 100901.

[30] N. Glück, T. Bein, *Energy Environ. Sci.* **2020**, *13*, 4691.

[31] R. E. Brandt, V. Stevanović, D. S. Ginley, T. Buonassisi, *MRS Commun.* **2015**, *5*, 265.

[32] Z. Xiao, W. Meng, J. Wang, D. B. Mitzi, Y. Yan, *Mater. Horiz.* **2017**, *4*, 206.

[33] P. Karuppuswamy, K. M. Boopathi, A. Mohapatra, H.-C. Chen, K.-T. Wong, P.-C. Wang, C.-W. Chu, *Nano Energy* **2018**, *45*, 330.

[34] M. Pazoki, M. B. Johansson, H. Zhu, P. Broqvist, T. Edvinsson, G. Boschloo, E. M. J. Johansson, *J. Phys. Chem. C* **2016**, *120*, 29039.

[35] Y. Peng, F. Li, Y. Wang, Y. Li, R. L. Z. Hoye, L. Feng, K. Xia, V. Pecunia, *Appl. Mater. Today* **2020**, *19*, 100637.

[36] F. Li, Y. Wang, K. Xia, R. L. Z. Hoye, V. Pecunia, *J. Mater. Chem. A* **2020**, *8*, 4396.

[37] M. B. Johansson, H. Zhu, E. M. J. Johansson, *J. Phys. Chem. Lett.* **2016**, *7*, 3467.

[38] Y. Lei, S. Wang, J. Xing, H. Xu, J. Han, W. Liu, *Inorg. Chem.* **2020**, *59*, 4349.

[39] C. Ji, P. Wang, Z. Wu, Z. Sun, L. Li, J. Zhang, W. Hu, M. Hong, J. Luo, *Adv. Funct. Mater.* **2018**, *28*, 1705467.

[40] B. Yang, Y. Li, Y. Tang, X. Mao, C. Luo, M. Wang, W. Deng, K. Han, *J. Phys. Chem. Lett.* **2018**, *9*, 3087.

[41] F. Jiang, D. Yang, Y. Jiang, T. Liu, X. Zhao, Y. Ming, B. Luo, F. Qin, J. Fan, H. Han, L. Zhang, Y. Zhou, *J. Am. Chem. Soc.* **2018**, *140*, 1019.

[42] J.-C. Hebig, I. Kühn, J. Flohre, T. Kirchartz, *ACS Energy Lett.* **2016**, *1*, 309.

[43] B.-W. Park, B. Philippe, X. Zhang, H. Rensmo, G. Boschloo, E. M. J. Johansson, *Adv. Mater.* **2015**, *27*, 6806.

[44] Z. Sun, A. Zeb, S. Liu, C. Ji, T. Khan, L. Li, M. Hong, J. Luo, *Angew. Chem., Int. Ed.* **2016**, *55*, 11854.

[45] B. Pradhan, G. S. Kumar, S. Sain, A. Dalui, U. K. Ghorai, S. K. Pradhan, S. Acharya, *Chem. Mater.* **2018**, *30*, 2135.

[46] Z. Zheng, Q. Hu, H. Zhou, P. Luo, A. Nie, H. Zhu, L. Gan, F. Zhuge, Y. Ma, H. Song, T. Zhai, *Nanoscale Horiz.* **2019**, *4*, 1372.

[47] P. Liu, Y. Liu, S. Zhang, J. Li, C. Wang, C. Zhao, P. Nie, Y. Dong, X. Zhang, S. Zhao, G. Wei, *Adv. Opt. Mater.* **2020**, *8*, 2001072.

[48] Z. Ji, Y. Liu, W. Li, C. Zhao, W. Mai, *Sci. Bull.* **2020**, *65*, 1371.

[49] A. A. Hussain, A. K. Rana, M. Ranjan, *Nanoscale* **2019**, *11*, 1217.

[50] D. Liu, B. Yu, M. Liao, Z. Jin, L. Zhou, X. Zhang, F. Wang, H. He, T. Gatti, Z. He, *ACS Appl. Mater. Interfaces* **2020**, *12*, 30530.

[51] D. Hao, D. Liu, Y. Shen, Q. Shi, J. Huang, *Adv. Funct. Mater.* **2021**, *31*, 2100773.

[52] X. Tong, Z. Zhang, D. Wang, L. Luo, C. Xie, Y. Wu, *J. Mater. Chem. C* **2019**, *7*, 863.

[53] W. Li, X. Wang, J. Liao, Y. Jiang, D. Kuang, *Adv. Funct. Mater.* **2020**, *30*, 1909701.

[54] Y. Zhang, Y. Liu, Z. Xu, H. Ye, Z. Yang, J. You, M. Liu, Y. He, M. G. Kanatzidis, S. Liu, *Nat. Commun.* **2020**, *11*, 2304.

[55] R. Liu, H. Zhou, R. Wang, D. Wu, X. Pan, G. Pan, H. Wang, *Sci. China Mater.* **2021**, *64*, 393.

[56] R. Zhuang, X. Wang, W. Ma, Y. Wu, X. Chen, L. Tang, H. Zhu, J. Liu, L. Wu, W. Zhou, X. Liu, Y. M. Yang, *Nat. Photonics* **2019**, *13*, 602.

[57] Z. Qi, X. Fu, T. Yang, D. Li, P. Fan, H. Li, F. Jiang, L. Li, Z. Luo, X. Zhuang, A. Pan, *Nano Res.* **2019**, *12*, 1894.

[58] W. Zhang, Y. Sui, B. Kou, Y. Peng, Z. Wu, J. Luo, *ACS Appl. Mater. Interfaces* **2020**, *12*, 9141.

[59] V. Vuong, S. V. N. Pammi, K. S. Pasupuleti, W. Hu, V. D. Tran, J. S. Jung, M. Kim, V. Pecunia, S. G. Yoon, *Adv. Opt. Mater.* **2021**, *9*, 2100192.

[60] R. H. Bube, *Photoelectronic Properties of Semiconductors*, Cambridge University Press, Cambridge, UK **1992**.

[61] A. Rose, *Concepts in Photoconductivity and Allied Problems*, Wiley and Sons, New York, USA **1963**.

[62] V. Pecunia, Y. Yuan, J. Zhao, K. Xia, Y. Wang, S. Duhm, L. Portilla, F. Li, *Nano-Micro Lett.* **2020**, *12*, 27.

[63] F. Umar, J. Zhang, Z. Jin, I. Muhammad, X. Yang, H. Deng, K. Jahangeer, Q. Hu, H. Song, J. Tang, *Adv. Opt. Mater.* **2019**, *7*, 1801368.

[64] P. Sebastia-Luna, M. C. Gélvez-Rueda, C. Dreessen, M. Sessolo, F. C. Grozema, F. Palazon, H. J. Bolink, *J. Mater. Chem. A* **2020**, *8*, 15670.

[65] J. P. Correa-Baena, L. Nienhaus, R. C. Kurchin, S. S. Shin, S. Wieghold, N. T. Putri Hartono, M. Layurova, N. D. Klein, J. R. Poindexter, A. Polizzotti, S. Sun, M. G. Bawendi, T. Buonassisi, *Chem. Mater.* **2018**, *30*, 3734.

[66] P. C. Harikesh, H. K. Mulmudi, B. Ghosh, T. W. Goh, Y. T. Teng, K. Thirumal, M. Lockrey, K. Weber, T. M. Koh, S. Li, S. Mhaisalkar, N. Mathews, *Chem. Mater.* **2016**, *28*, 7496.

[67] B. Chabot, E. Parthé, *Acta Crystallogr., Sect. B: Struct. Sci., Cryst. Eng. Mater.* **1978**, *34*, 645.

[68] A. Singh, K. M. Boopathi, A. Mohapatra, Y. F. Chen, G. Li, C. W. Chu, *ACS Appl. Mater. Interfaces* **2018**, *10*, 2566.

[69] K. Yamada, H. Sera, S. Sawada, H. Tada, T. Okuda, H. Tanaka, *J. Solid State Chem.* **1997**, *134*, 319.

[70] T. D. Chonamada, A. B. Dey, P. K. Santra, *ACS Appl. Energy Mater.* **2020**, *3*, 47.

[71] B. Saparov, F. Hong, J. P. Sun, H. S. Duan, W. Meng, S. Cameron, I. G. Hill, Y. Yan, D. B. Mitzi, *Chem. Mater.* **2015**, *27*, 5622.

[72] S. Berri, *Eur. Phys. J. B* **2020**, *93*, 191.

[73] K. M. McCall, C. C. Stoumpos, S. S. Kostina, M. G. Kanatzidis, B. W. Wessels, *Chem. Mater.* **2017**, *29*, 4129.

[74] K. M. McCall, C. C. Stoumpos, O. Y. Kontsevoi, G. C. B. Alexander, B. W. Wessels, M. G. Kanatzidis, *Chem. Mater.* **2019**, *31*, 2644.

[75] V. Pecunia, J. Zhao, C. Kim, B. R. Tuttle, J. Mei, F. Li, Y. Peng, T. N. Huq, R. L. Z. Hoye, N. D. Kelly, S. E. Dutton, K. Xia, J. L. MacManus-Driscoll, H. Sirringhaus, *Adv. Energy Mater.* **2021**, *11*, 2003968.

[76] S. M. Sze, K. K. Ng, *Physics of Semiconductor Devices*, 3rd ed., John Wiley & Sons, Inc., Hoboken, NJ, USA **2006**.

[77] P. Schulz, D. Cahen, A. Kahn, *Chem. Rev.* **2019**, *119*, 3349.

[78] L. E. Polander, P. Pahner, M. Schwarze, M. Saalfrank, C. Koerner, K. Leo, *APL Mater.* **2014**, *2*, 081503.

[79] X. Jiang, D. Wang, Z. Yu, W. Ma, H. B. Li, X. Yang, F. Liu, A. Hagfeldt, L. Sun, *Adv. Energy Mater.* **2019**, *9*, 1.

[80] A. Köhler, H. Bässler, in *Electronic Processes in Organic Semiconductors*, Wiley-VCH Verlag GmbH & Co. KGaA, Weinheim, Germany **2015**, pp. 307–388.

[81] J. Zhao, P. Wang, L. Wei, Z. Liu, X. Fang, X. Liu, D. Ren, Y. Mai, *Dalton Trans.* **2015**, *44*, 16914.

[82] N. Osterthun, N. Neugebohrn, K. Gehrke, M. Vehse, C. Agert, *Opt. Express* **2021**, *29*, 938.

[83] R. S. Crandall, *J. Appl. Phys.* **1983**, *54*, 7176.

[84] H. Azimi, T. Ameri, H. Zhang, Y. Hou, C. O. R. Quiroz, J. Min, M. Hu, Z. G. Zhang, T. Przybilla, G. J. Matt, E. Spiecker, Y. Li, C. J. Brabec, *Adv. Energy Mater.* **2015**, *5*, 1401692.

[85] T. Kirchartz, T. Agostinelli, M. Campoy-Quiles, W. Gong, J. Nelson, *J. Phys. Chem. Lett.* **2012**, *3*, 3470.

[86] R. H. Bube, *Photoconductivity of Solids*, John Wiley & Sons, Inc, New York, USA **1960**.

[87] A. Rose, *RCA Rev.* **1951**, *12*, 362.

[88] *Photonic Devices*, (Ed: J. Liu), Cambridge University Press, Cambridge, UK **2005**, pp. 926–1017.

[89] A. Armin, M. Hambsch, I. K. Kim, P. L. Burn, P. Meredith, E. B. Namdas, *Laser Photonics Rev.* **2014**, *8*, 924.

[90] M. Liu, J. Wang, Z. Zhao, K. Yang, P. Durand, F. Ceugniet, G. Ulrich, L. Niu, Y. Ma, N. Leclerc, X. Ma, L. Shen, F. Zhang, *J. Phys. Chem. Lett.* **2021**, *12*, 2937.

[91] K. Yang, J. Wang, Z. Zhao, Z. Zhou, M. Liu, J. Zhang, Z. He, F. Zhang, *ACS Appl. Mater. Interfaces* **2021**, *13*, 21565.

[92] K. Xia, Y. Li, Y. Wang, L. Portilla, V. Pecunia, *Adv. Opt. Mater.* **2020**, *8*, 1902056.

[93] Z. Li, G. Lakhwani, N. C. Greenham, C. R. McNeill, *J. Appl. Phys.* **2013**, *114*, 034502.

[94] Z. Li, C. R. McNeill, *J. Appl. Phys.* **2011**, *109*, 074513.

[95] F. Gao, Z. Li, J. Wang, A. Rao, I. A. Howard, A. Abrusci, S. Massip, C. R. McNeill, N. C. Greenham, *ACS Nano* **2014**, *8*, 3213.

[96] P. W. Kruse, in *Optical and Infrared Detectors*, (Ed: R. J. Keyes), Springer, Berlin, Germany **1977**, pp. 5–70.

[97] C. C. Boyd, R. C. Shallcross, T. Moot, R. Kerner, L. Bertoluzzi, A. Onno, S. Kavadiya, C. Chosy, E. J. Wolf, J. Werner, J. A. Raiford, C. de Paula, A. F. Palmstrom, Z. J. Yu, J. J. Berry, S. F. Bent, Z. C. Holman, J. M. Luther, E. L. Ratcliff, N. R. Armstrong, M. D. McGehee, *Joule* **2020**, *4*, 1759.

[98] Y. Liu, J. Zhang, H. Wu, W. Cui, R. Wang, K. Ding, S. T. Lee, B. Sun, *Nano Energy* **2017**, *34*, 257.